Low Spring Index NiTi Coil Actuators for Use in Active Compression Garments

Bradley Holschuh, Edward Obropta, and Dava Newman

***Abstract*—This paper describes the modeling, development, and testing of low spring index nickel titanium (NiTi) coil actuators designed for use in wearable compression garments, and presents a prototype tourniquet system using these actuators. NiTi coil actuators produce both large forces (>1 N) and large recoverable displacements (>100% length) that are well suited for compression garment design. Thermomechanical coil models are presented that describe temperature and force as a function of non-dimensionalized coil geometry, extensional strain, and applied voltage. These models suggest that low spring index coils maximize activation force, and an analytical model is presented to predict garment counter-pressure based on actuator architecture. Several low spring index (C = 3.08) coils were manufactured, annealed, and tested to assess their de-twinning and activation characteristics. Results suggest both annealing and applied stress affect activation thresholds. Actuator force increases both with extensional strain and applied voltage up to 7.24 N. A first-generation compression tourniquet system using integrated actuators with direct voltage-control of applied pressure is presented, demonstrating >70% increase in applied pressure during activation. This approach enables new, dynamic garments with controllable activation and low effort donning and doffing, with applications ranging from healthcare solutions to advanced space suit design.**

***Index Terms*—Shape memory alloy (SMA) actuators, nickel titanium (NiTi) coil springs, controllable compression garment design, active materials, smart textiles.**

I. Introduction

COMPRESSION garments serve many functions in our daily lives. Compression stockings are used regularly to help patients suffering from venous insufficiency or to manage lymphedema [1], [2]; athletes don specifically engineered compression shorts to improve athletic performance and to increase comfort during workouts [3]; pressure garment therapy has been used to support burn victim recovery for over 50 years [4]; and cosmetic shapewear compression garments have recently exploded in popularity among those looking for a more streamlined figure. Compression garments also see use in extreme environment situations. The US military uses compression garments for emergency battlefield medicine [5]; and NASA and its partner universities have been investigating compression technologies for decades both as a countermeasure against post-spaceflight orthostatic intolerance in astronauts [6] and for use in lightweight, full-body, high-mobility compression suits known as a mechanical counter-pressure (MCP) suits for future planetary exploration [7]–[11].

Compression garments typically take the form of either tight fitting elastic materials (in the case of [1]–[4], [7]–[11]) or as an inflatable bladder system (in the case of [2], [6]). Both designs offer unique benefits and disadvantages. Inflatable systems are adjustable (i.e., the magnitude and location of counter-pressure can be controlled by adjusting the inflation characteristics), but they require bulky plumbing, are subject to leaks, can be very costly, and require access to high pressure gas sources to function [2], [6]. Elastic systems are form fitting, lightweight and streamlined, but are generally static in design (i.e., the amount of pressure produced on a given object is unchanging, and is a direct function of the material properties and the shape/size of the garment relative to the wearer), offer no controllability, and can be difficult to don/doff [7]–[11]. In the specific case of MCP suits for space exploration, neither design suffices, as the bulkiness and mobility restrictions of an inflatable garment are prohibitive, and the static nature of an elastic garment combined with the high material tension required to provide adequate life support makes donning/doffing arduous [7]–[10].

In this paper we investigate the use of active materials in compression garment design to improve functionality for both everyday uses and for extreme environment situations. Active materials are a category of materials that react to an applied stimulus, resulting in dimensional changes that produce controllable forces and displacements [12]. Many of these materials are commonly referred to as artificial muscles for their use in robotic actuation systems, as their behavior is designed to mimic human muscle [12]. By incorporating such shape change materials into a wearable garment, we seek to develop garments capable of changing shape on command, providing the controllability and ease of donning/doffing of an inflatable compression garment with the lightweight, form-fitting characteristics of a passive elastic garment.

Many different types of active materials exist, including (but not limited to) shape memory alloys (SMAs), shape memory polymers (SMPs), dielectric elastomer actuators (DEAs), piezoelectrics, ionic polymer metal composites (IPMCs), ferroelectric polymers, and have even expanded to include inexpensive polymer fibers like those used for fishing line and sewing thread [12]–[14]. Each material exhibits different characteristics, form factors, and stimulation mechanisms (thermal, electrical, magnetic, etc.). An ideal active material candidate for integration into a wearable compression garment would meet the following criteria:

Manuscript received 11/04/2013; accepted 05/07/2014. This work is supported in part by the National Aeronautics and Space Administration (NASA) Office of the Chief Technologist (OCT) under Grant NNX11AM62H, and by the MIT Portugal Program (MPP).

B. Holschuh, E. Obropta and D. Newman are with the Department of Aeronautics and Astronautics, Massachusetts Institute of Technology, Cambridge, MA, 02139 USA (e-mail: holschuh@mit.edu; eobropta@mit.edu; dnewman@mit.edu).

1) Can repeatably generate high forces and have the ability to produce large displacements when stimulated
2) Can be packaged or integrated into a textile structure easily and without adding significant bulk or mass
3) Can be stimulated in a way that is both feasible and safe for the wearer

Given these requirements, many of the available active material candidates are currently ill-suited for the task (e.g., carbon nanotubes exhibit active strains of $<1\%$, an impractically small activation stroke for the purpose of producing compression, and ferroelectric polymers often require bulky magnets) [12]. DEAs, SMPs, and SMAs all theoretically meet the minimum active stress requirements to achieve MCP design specifications (29.6 kPa) with at least single-digit active strains and form factors suitable for wearable systems [9], [10], [12], [15], [16]. Initial investigations into these materials suggest that DEAs and SMPs, in their current technical state, suffer from significant performance limitations: DEAs were shown to have very limited durability while requiring high (i.e., >1 kV) activation voltages [17], [18]; SMPs were shown to be deficient as they experience significant viscoelastic and irrecoverable strain effects [19]. Consequently, in this paper we investigate shape memory alloys (SMA) as the top choice for actuators in a controllable compression garment architecture. We describe the modeling, development, testing and prototype integration of SMA nickel titanium (NiTi) actuators specifically tailored for compression garment applications. The actuators described are engineered with a specific coil geometry based on modern SMA coil design criteria, and are tailored to meet the specifications of high force, large stroke compression garments like those of an MCP space suit. We demonstrate the ability of these actuators to be integrated into an architecture that provides controllable compression in combination with passive elastic materials.

The contributions of this research effort include:

1) A novel SMA coil actuator design, including force and thermal modeling methods, for the purpose of designing high force, large displacement linear actuators for use in wearable garments and advanced space suit design
2) A non-dimensionalized model for predicting counter-pressure based on actuator parameters and architectures, and an assessment of the controllability and scalability of linear actuation systems using these coil actuators
3) A demonstration of an integrated, controllable active tourniquet compression prototype, with discussion on expanded design options for a variety of controllable compression garment architectures

This paper is organized into the following sections: in Section II we describe the state of force and thermal modeling of NiTi coil actuators, present a nondimensionalized analytical model for predicting garment counter-pressure given a variety of design parameters, and discuss how these models inform the design of actuators suited for compression textiles; in Section III we detail the manufacturing and annealing techniques used to produce low spring index coil actuator test specimens; in Section IV we describe the experimental characterization of the NiTi actuators with comparisons to model predictions; in Section V we present the design of an integrated, controllable active tourniquet system utilizing our embedded actuator technology, and describe its performance; and Section VI culminates in a discussion of active compression garment design based on the results of this research effort.

II. Theory and Modeling of NiTi Coil Actuators

SMAs exhibit thermally induced shape recovery capabilities as a result of solid state diffusionless phase transformations [12], [20]. As SMAs are heated, they transform from the low-temperature, face-centered tetragonal lattice martensite phase to the high-temperature, body-centered cubic lattice austenite phase. In the absence of external stress, this phase transformation drives a repeatable macro-scale shape change, and both the memory shape and activation temperature thresholds can be tailored for custom applications (by annealing the alloy while fixed in the desired shape, or by modifying the alloy mixture, respectively) [20].

Several alloys exhibit this type of memory characteristic, though NiTi is the most widely studied and is used commercially for a variety of applications [12], [20]. NiTi memory elements have been used (among other things) in: stents [21]; catheters [22]; actuators for robotic and biomimetic systems [23]–[27]; morphing aircraft structures [20]; orthopedic implants [20]; systems for structural health monitoring [28]; robotic pumps [29]; and even as integrated elements in clothing [30]. SMAs offer high blocking stresses (200 MPa), high specific power (>100 kW/kg), and can be actuated using Joule heating via an applied current [12]. Drawbacks of NiTi and other SMA actuators include low efficiencies, slow response times (as they rely on heat transfer for actuation and cooling), difficulties in precision control in thermally dynamic environments, and moderately small (i.e., typically 1-8%) active strains [12].

To address the problem of small active strains exhibited by SMAs, designers have often trained NiTi wires as coil actuators, such that activation leads to either expansion or contraction of the coil structure [31]–[36]. A depiction of a typical SMA coil actuation cycle is included in Fig. 1. First, a raw NiTi wire is wound into a coil configuration and annealed at high temperature to set the austenite memory state. Once the coil is cooled (either by water quenching or by free convective cooling) it transforms to the twinned martensite state. This represents the beginning state of a repeatable three-step activation cycle. First, an external force deforms and extends the coil, causing de-twinning of the crystal structure. Next, the coil is heated above the austenite start and stop temperatures, resulting in contraction as austenite phase transformation occurs. Finally, the coil cools, re-entering the twinned martensite phase, allowing the cycle to repeat. This can be understood in terms of stress, strain, and temperature using Fig. 2.

NiTi coils can achieve displacements that are orders of magnitude greater ($>100\%$) than those of a typical axially-aligned SMA wire [25], [35]. The combination of high forces, large displacements, simple activation mechanism, low mass, compact form factor and fiber-like aspect ratio make NiTi

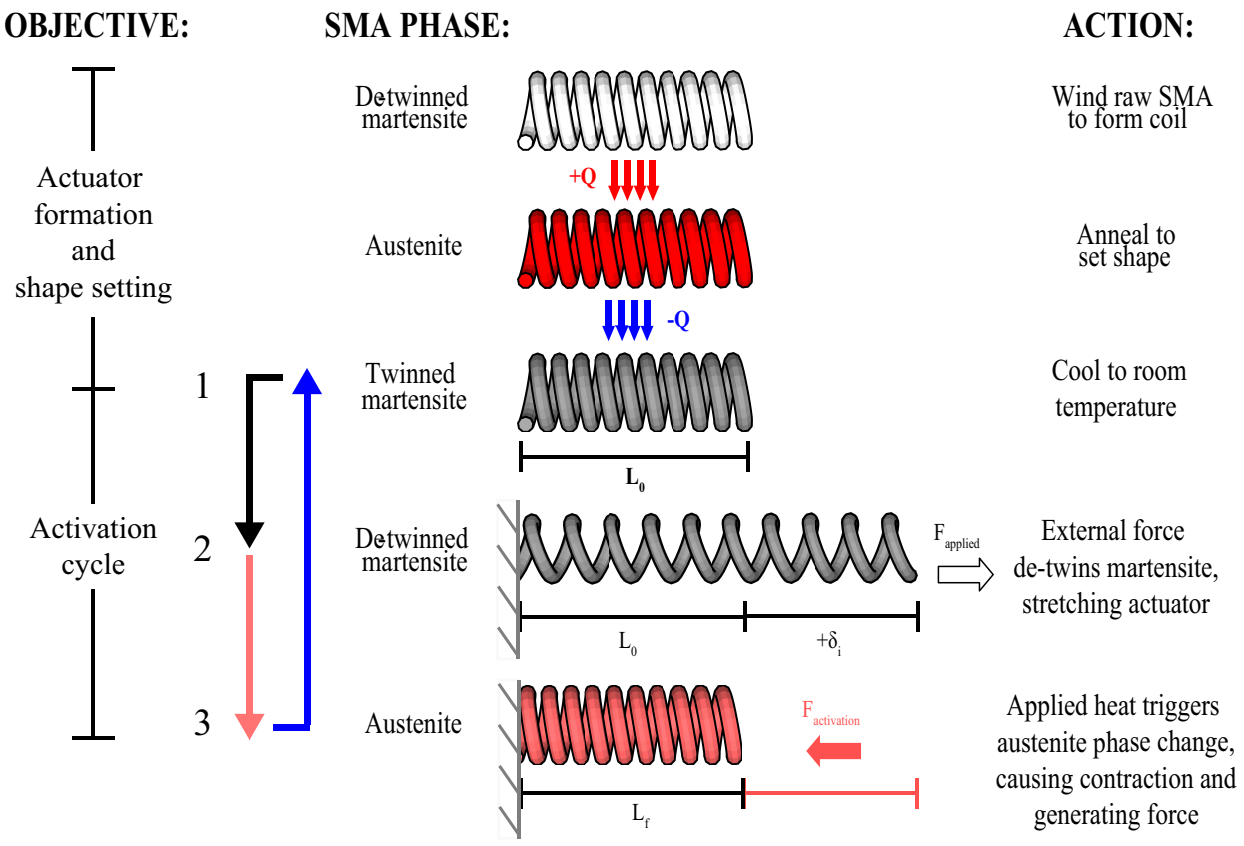

Fig. 1. SMA coil actuator shape setting steps and activation cycle. Once a coil has been wound and annealed, it follows a 3-step activation cycle: a shape-set twinned martensite actuator is subjected to an external force, causing martensite de-twinning; the actuator is heated, and austenite phase-change occurs leading to activation; subsequent cooling causes martensite phase-change, ending in the original twinned state.

SMA coil structures well-suited for inclusion in an active compression textile.

A. Geometry and Force Modeling of NiTi Coils

NiTi compression coils are defined by several geometric parameters, presented in Fig. 3: NiTi wire diameter d; spring diameter D, as measured by the midpoint between inner and outer diameters; number of active coils n; solid spring length L_s, defined as the length of a spring that is fully packed; free spring length L_0, defined as the zero-load length of the spring (and for our purposes, the length of the SMA actuator when fully actuated with no load); spring pitch p, defined as the distance between adjacent coils; spring pitch angle α, defined as the angle between a given coil and the local horizontal; initial and final extended spring length, L_i and L_f, defined in this case as the total extended spring length pre- and post-activation (under no load, $L_f \simeq L_0$); initial and final linear displacement δ_i and δ_f, defined as the difference between initial and final extended spring length and free spring length; and spring index C, defined as the ratio of spring diameter to wire diameter.

The force F generated by a NiTi coil with a given set of geometric parameters and a known shear modulus G follows Hooke's law, and can be expressed in simplified form as follows [25], [31], [32]:

$$F = kx = k\delta \tag{1}$$

where

$$k = \frac{Gd^4}{8D^3n}. \tag{2}$$

Substituting (2) into (1), and applying the definition of spring index C, the activation force relationship becomes:

$$F = \frac{Gd}{8C^3n}\delta. \tag{3}$$

Recent studies have proposed modifications to (3) to more accurately capture the changes to coil geometry that manifest as displacement increases. An *et al.* proposes a two-state NiTi coil model modified from the conventional force-displacement model, where G_M and G_A (martensite and austenite shear moduli) are used to describe the system response in either the pure martensite or austenite phase, with additional terms to account for reductions in spring diameter during large displacements, and for de-twinning and bending moment effects [31]. Seok *et al.*'s enhanced model accounts for changes in free length of the spring due to phase transition [25].

The basic model described in (3) is sufficient to analyze the relationship between coil parameters and actuator performance. We seek to maximize force per actuator when designing coils for use in a compression garment system to

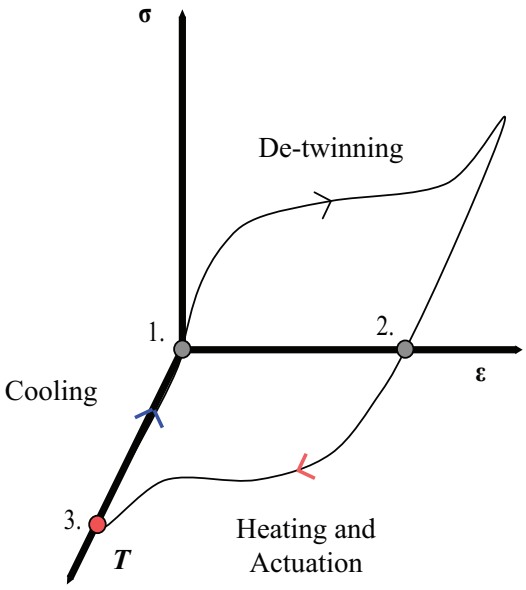

Fig. 2. Activation cycle depicted graphically in terms of stress, strain, and temperature, for a hypothetical zero-load system [20].

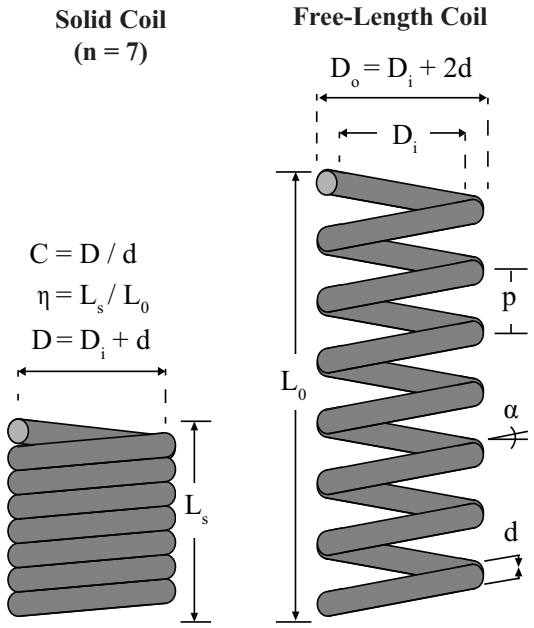

Fig. 3. Spring parameters as defined by coil geometry, for both a fully compressed (solid) spring and a free-length spring.

maximize the magnitude of active pressure produced (which is a function of the hoop stress generated) while minimizing the number of active elements, and (3) provides several insights into optimal actuator design. First, because n, L_0, and δ are physically linked quantities, we can modify (3) by defining two non-dimensionalized parameters: packing density, η, and actuator extensional strain, ϵ. We define packing density η as the ratio of the number of active coils n contained in the free spring length L_0 relative to the physical limit. This can also be defined as the ratio of the solid spring length to the free spring length (or the ratio of solid spring pitch, which is simply d, to free spring pitch):

$$\eta = \frac{d}{p} = \frac{L_s}{L_0} = \frac{nd}{L_0}. \tag{4}$$

Second, we define actuator extensional strain ϵ as the ratio of spring displacement δ to free spring length L_0 (note that extensional strain in this context captures changes in linear distance of the total actuator, and not the axial deformation of the constituent NiTi metal itself, which is the typical usage of the term strain):

$$\epsilon = \frac{\delta}{L_0}. \tag{5}$$

In Fig. 3, we see that for a given L_0, $\eta \leq 1$, with $\eta = 1$ when $L_0 = L_s$ (and therefore $p = d$). It is important to note that the quantity L_0, which we previously defined as the length of the actuator when fully actuated with no load, changes over the lifespan of an actuator as fatigue effects set in (i.e., cycling will cause the activated length to creep when compared to the free length at the time of annealing); because both η and ϵ rely on L_0, these values also creep over time, and care must be taken to be sure that the current L_0 is known before performing specific calculations. By substituting (4) and (5) into (3), we can define the force output of a given actuator in terms of coil density and extensional strain (which are both non-dimensional terms), rather than δ (which has the dimension of distance) and n. This is useful for design purposes, and results in the following final form:

$$F = \frac{Gd^2}{8C^3\eta}\epsilon. \tag{6}$$

Equation (6) is defined purely in terms of coil packing density, extensional strain, spring index, and wire diameter, rather than by specific values of active coils and displacements. We see that for a given extensional strain ϵ, force per actuator is maximized when η is minimized, and that force increases linearly with ϵ. These relationships suggest designs that use short actuators extended to their extensional strain limit prior to actuation (i.e., de-twinned to at least point 2 in Fig. 2). According to (6), such designs will produce the greatest force per actuator for a desired initial extensional strain. However, the quantities η and ϵ are physically linked: maximum extensional strain decreases as packing density decreases (and vice versa) because each active coil has an upper limit in terms of achievable pitch angle, so actuators with low starting packing densities (and thus higher starting pitch angles) will encounter their extensional strain limit at lower values. Tradeoffs between maximum force for a given final extensional strain (which is important for pressure generation and is achieved by minimizing packing density for a given L_0), and maximum initial extensional strain capability (which is important for increased ease of donning/doffing and is achieved by maximizing packing density for a given L_0) must be considered individually for each application.

We also see that for a given NiTi wire diameter, force is maximized by minimizing spring index. Spring index is a measure of the sharpness of curvature of a given coil, and a physical limit exists below which the metal experiences

cracking and other structural damage, and specialized equipment is necessary for manufacturing. Recommendations for spring design list a minimum spring index of 3 to avoid these issues [37]–[39], producing a stiffer spring and increased shear stress as defined by the Wahl correction factor [25]. However, minimizing spring index has the desirable effect of maximizing actuator aspect ratio (as defined as spring length/width), bringing the actuator form factor closer to a typical textile fiber.

Updating (6) with the minimum spring index value (C = 3) results in the final force equation for a low spring index coil actuator:

$$F = \frac{Gd^2}{216\eta}\epsilon. \tag{7}$$

Finally, force increases with the square of NiTi wire diameter, suggesting designs that employ thick wires. However, coil diameter also increases linearly with wire diameter for a fixed spring index, which may introduce design limits if space is tight for a particular design, so wire diameter may be constrained by application geometry.

Taking each of these relationships into account, to size an optimized actuator system (i.e., number of parallel actuators $n_{actuator}$ that each produce a maximum activation force F_{max}) for use in a textile compression system to achieve a counter-pressure target P over a local limb radius r, we calculate the tension force T per axial width w according to the thin-walled hoop stress equation using the following equation: [10]:

$$Pr = \frac{T}{w} = \frac{F_{max} n_{actuator}}{w} \tag{8}$$

This conceptual configuration is depicted graphically in Fig. 4. Note that (8) uses the maximum force generated by a single actuator, which is determined by (7) using the pure austenite shear modulus value at a given final (i.e., post-activation) extensional strain. Further, assuming a standard single-layer, parallel actuator configuration, the upper limit of total actuators will be constrained by the total axial width and by the fixed spring index:

$$w \geq (D + d)(n_{actuator}) = 4d(n_{actuator}). \tag{9}$$

Substituting (7) and (9) into (8) and rearranging we are left with the following equation for maximum counter-pressure that can be produced using low spring index coils:

$$P \leq \frac{G_A d \epsilon_f}{864 r \eta}. \tag{10}$$

We see in (10) that maximum counter-pressure scales with SMA wire thickness and actuator extensional strain, is inversely proportional to limb radius and coil packing density, and can be achieved over any width (so long as it is an integer multiple of the outer diameter of the chosen actuator). Putting (10) into practice using real-world values, for an average human thigh radius (9.5 cm), a typical G_A value (30 GPa), a commercially-available SMA wire diameter (305 μm) and reasonable estimates for coil packing density and actuator extensional strain (0.9 and 0.5, respectively) we

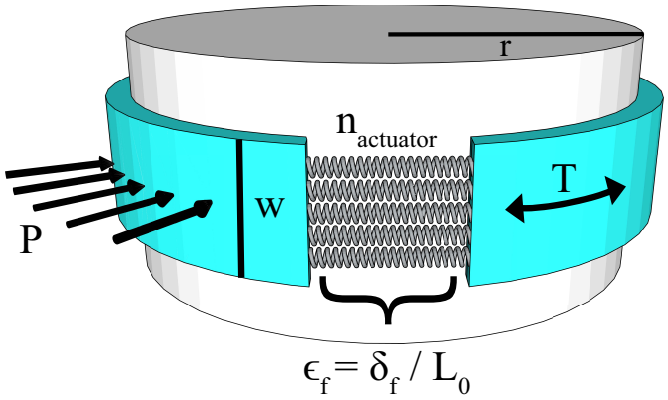

Fig. 4. Schematic of the variables that determine counter-pressure applied by a thin vessel on a solid surface based on the general hoop stress equation using the thin-walled pressure vessel assumption. A proposed architecture of several low spring index NiTi coils aligned in a single, circumferentially-aligned parallel layer is presented.

can theoretically produce counter-pressure magnitudes over an arbitrary thigh width as follows [31], [40]:

$$P \leq \left(\frac{(30 \cdot 10^9 \text{Pa})(305 \cdot 10^{-6} \text{m})(0.5)}{(864)(0.095\text{m})(0.9)}\right) = 61.9\text{kPa}. \tag{11}$$

We see that the counter-pressure design goal for an MCP space suit, 29.6 kPa [7]–[11], is well within the theoretical capability of a parallel array of low spring index SMA coil actuators (for even the thigh, which is the largest average human limb radius), and that performance can be tuned based on actuator extensional strain, SMA wire thickness, and designed coil actuator packing density.

Note that (10) and (11) assume that the maximum possible force is generated by the embedded SMA actuator subsystem. In order for this assumption to be valid, several conditions must be met: the actuators must be arranged in a single parallel layer; perfect actuator spacing must be achieved (i.e., no wasted space between adjacent actuators); and complete austenite phase transformation of all actuators must be achieved. If the SMAs are not arranged in a single parallel layer, the geometric relation expressed in (9) does not hold, and a new relation between actuator number and compression band width must be derived and substituted into (8). If actuator spacing is not optimized, the inequality forms of (9) and (10) hold, and (9) must be modified to better reflect the actual number of actuators contained in the compression band width if an explicit pressure prediction is desired. If complete austenite phase transformation is not achieved, the austenite shear modulus term in (10) must be modified (i.e., reduced) to reflect the actual material condition.

B. Thermal Modeling of NiTi Coils

Thermal activation of NiTi coils is generally achieved through Joule heating (i.e., the heat generated as current passes through a resistor). This provides a direct and controllable input mechanism for SMA activation. To fully model this phenomenon, 5 terms must be considered: power input from

the applied voltage; conductive heat flow through the wire; convective heat loss to the environment; transformation heat flux associated with the phase change during activation; and radiation heat loss [27], [41]–[43]. Equation (12) provides a simplified baseline model that disregards radiation and transformation heat flux effects (but is analytically solvable):

$$\frac{U^2}{R(T)} = hA(T(t) - T_\infty) + \rho V c_p \frac{dT}{dt}. \tag{12}$$

In this equation: U is the applied voltage; R is the wire resistance as a function of wire temperature T; h is the heat transfer coefficient; A is the surface area of the wire; T is the wire temperature as a function of time; T_∞ is the ambient temperature; c_p is the specific heat of NiTi; V is the volume of the wire; and ρ is the density of NiTi. NiTi resistivity is dependent on the fraction of austenite and martensite in the material, which changes as the wire is actuated [44], though previous studies have found this effect to be small enough to disregard [41]. Additionally, as NiTi wire actuates it does slightly change length (average active strain is $\leq$ 5% [12]), which would affect the volume, surface area, and density terms, though these effects are also assumed to be negligible.

By assuming that wire resistivity can be simplified to the resistivity of pure austenite NiTi, (12) can be simplified and rearranged to solve for coil temperature as a function of time and applied voltage:

$$T(t) = \frac{U^2}{hAR}\left(1 - e^{\frac{-hA}{\rho V c_p}\cdot t}\right) + T_\infty. \tag{13}$$

Using (13) in combination with (10), and knowing the activation temperature thresholds and behavior of a given NiTi coil actuator, it becomes possible to predict its voltage-extensional strain-force/pressure characteristics.

III. NiTi Coil Manufacturing and Shape Setting

To manufacture low spring index actuators, we adapted the method developed by Kim *et al.* [32] and Seok *et al.* [25]. First, the low spring index spring form is established prior to annealing by winding 305 μm (0.012") NiTi Flexinol muscle wire [Dynalloy Inc.] around a 635 μm (0.025") stainless steel core, resulting in a spring index C $\sim$ 3.08. Winding is accomplished by hanging the steel core under tension from a variable speed DC motor, and progressively feeding the NiTi wire along the length of the core using a packing rod as the core rotates. Downward tension is induced in the NiTi wire manually, and upward tension is provided by the packing rod at the point of winding to ensure tight packing density and consistent pitch angle. This method, which is represented in Fig. 5(a), was found to repeatably produce coils with average η = 0.887 ($\pm$ 0.02, at 95% confidence).

The specific NiTi wire diameter (305 μm) selected is a compromise between maximum force (and therefore maximum pressure) and coil thickness (coil outer diameter, in this case OD $\sim$ 1.25 mm, determines the bulkiness of the actuator system relative to the passive textile thickness). There is evidence that as-drawn Nitinol provides larger deflections for a given force and spring shape [26] and is significantly cheaper than Flexinol muscle wire; however, Flexinol was chosen based on previous research that served to best inform our annealing parameters [25].

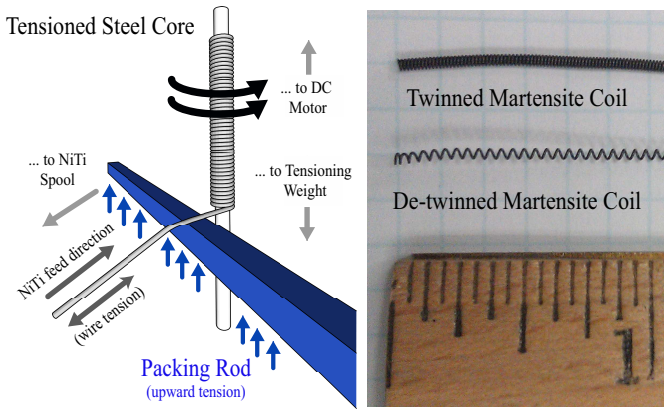

Fig. 5. A (left): winding method to produce low spring index NiTi coil actuators, adapted from Seok *et al.* and Kim *et al.* [25], [32]. B (right): actual low spring index NiTi coils (twinned martensite coil shown above, and de-twinned martensite coil below).

Once wound at room temperature, each coil is clamped on both ends to retain its shape and annealed at 450°C for 10 minutes to set the austenite memory state, after which it is water quenched and the steel core and clamps are removed. These annealing parameters were selected as a balance between minimizing de-twinning force and minimizing permanent plastic deformation after actuation [25]. Examples of finished twinned and de-twinned actuators are included as Fig. 5(b).

IV. Fundamental NiTi Coil Characterizations

A. Differential Scanning Calorimetry (DSC) Testing

Calorimetry analysis using a Mettler thermogravimetric analyzer/differential scanning calorimetry machine (TGA/DSC 1) [Mettler Toledo International Inc.] was performed to determine the stress-free critical temperatures (austenite start and finish temperatures, A_s and A_f, and martensite start and finish temperatures, M_s and M_f) of both raw Flexinol NiTi wire and our custom annealed coils. Five samples (2 raw Flexinol wire samples, and 3 annealed coil samples) were individually heated from 20°C to 195°C, then cooled from 195°C to 35°C, at a rate of 5°C/min, and normalized heat flow (W/g) was measured at 2 Hz. Each test was repeated twice for comparison, resulting in 20 total datasets (10 martensite to austenite transformations, and 10 austenite to martensite transformations). Critical temperatures were visually identified as the temperatures that mark the beginning and end of spikes in heat flow (signaling an endo- or exo-thermic process that stems from an internal phase change during activation), with an estimated uncertainty of $\pm 5°$ [20].

The results of these tests are shown in Table I. The specific raw Flexinol specimens tested are reported by the manufacturer to actuate at 70°C, and we see that in both the de-twinned and twinned starting condition, the raw wire austenite finish temperature is near that value (austenite starting temperature is significantly lower, and varies depending on whether the

TABLE I
SUMMARY OF NITI COIL CALORIMETRY ANALYSIS: ESTIMATED ACTIVATION TEMPERATURES (±5°) FOR RAW, ANNEALED SPECIMENS

Material Type	Martensite Starting State	A_S [°C]	A_F [°C]	M_S [°C]	M_F [°C]
Raw Flexinol	De-Twinned	63.3	74.2	81.4	–
Raw Flexinol	Twinned	41.3	75.3	83.5	–
Annealed Coil	De-Twinned	48.5	69.8	50.7	39.3
Annealed Coil	Twinned	44.1	58.4	49.6	39.5

sample begins de-twinned or twinned). When cooling raw wire from the activated (austenite) state, we see that martensite transformation begins near the reported activation temperature (approximately 80°C), though it does not fully complete at temperatures as low as 35°C (explaining the voids in Table I, indicating the final transformation temperature is <35°C). We see different behavior for annealed coil samples: the austenite activation window (start and stop temperatures) is downshifted, and the martensite activation window begins at a significantly lower temperature and is completed at approximately 39°C.

Accounting for the effect of multiple comparisons using the Bonferonni correction, the dataset shows no statistically significant effects due to annealing or martensite starting state. Annealing appears to affect critical temperatures for both de-twinned and twinned samples, as does starting martensite condition on austenite start temperatures, but these effects were not found to be significant given the small dataset and the large uncertainties in the estimated transformation temperatures. Previous studies have found initial martensite state (de-twinned vs. twinned) and annealing history to be statistically significant influences on SMA activation behavior; however, additional data collection and analysis is necessary before these effects can be demonstrated in the data [20].

B. Martensite De-twinning Force Testing

To characterize the de-twinning behavior of the NiTi coil actuators, tensile tests were performed using a Zwick/Roell tensile test machine [Zwick GmbH & Co.]. For each test, a twinned martensite coil was placed into the test machine, with clamps used to hold the coil in place at both ends. The coil was then stretched to 150% of its initial length (i.e., ϵ = 1.5) at a constant rate of 10 mm/min and tensile force was recorded. Tests were repeated twice on 25, 30, and 35 mm actuators, for a total of 6 tests. Shear stress τ and shear strain γ were determined using the initial pitch angle α_i, the final pitch angle α_f, Poisson's ratio v, and the known spring index [31]:

$$\tau = \frac{8CF}{\pi d^2}; \tag{14}$$

$$\gamma = \frac{1}{C}\left(\frac{cos^2\alpha_i(sin\alpha_f - sin\alpha_i)}{cos^2\alpha_f(cos^2\alpha_f + sin^2\alpha_f/(1+v))}\right). \tag{15}$$

The two-state martensite model from An *et al.* [31], which uses the residual strain γ_L and shear-stress induced de-twinned martensitic volume fraction $\psi_{S\tau}$, was used to compare the experimental results between studies:

TABLE II
COMPARISON OF TWO-STATE MODEL PARAMETERS

Data	G_M [MPa]	τ_s [MPa]	τ_f [MPa]	γ_L
An *et al.*	6980	72.4	114	0.05
An *et al.**	8932	43.4	86.45	0.045

$$F = \frac{G_M d}{8C^3 n}\left(\frac{cos^3\alpha_i}{cos^2\alpha_f(cos^2\alpha_f + sin^2\alpha_f/(1+v))}\right)\delta - \frac{\pi d^3}{8D}G_M\gamma_L\psi_{S\tau} \tag{16}$$

where

$$\psi_{S\tau} = \frac{1}{2}cos\left[\frac{\pi}{(\tau_s - \tau_f)}(\tau - \tau_f)\right] + \frac{1}{2}. \tag{17}$$

The results of the de-twinning tests are included in Fig. 6, which shows how shear stress varies with respect to shear strain (data is presented as the average over 6 tests, with 95% confidence bounds). Each coil undergoes three distinct regimes as it de-twins: the first regime of the curve is a linear, elastic response, while the coil is still twinned; the second regime, and the first non-linearity, corresponds to the de-twinning process; and the final regime, and second linearity, corresponds to the elastic de-twinned response [31]. A coil stretched through this process will remain de-twinned until thermal re-activation, resulting in irrecoverable extensional strains measured up to approximately 200% of starting length (ϵ = 2).

The parameters for the two state model, as reported by An *et al.* and as calculated based on our experimental data, are displayed in Table II. Fig. 6 demonstrates that the two state model developed by An *et al.* holds for our coil actuators, which are lower spring index and ten times longer than those used in their study.

C. Active Blocking Force Thermal Testing

To characterize the blocking force response of the coil actuators (i.e., the force generated by a coil actuator when held at a fixed displacement when activated), multiple actuators were stretched to 100% their initial length (i.e., ϵ = 1) using a Zwick/Roell tensile test machine equipped with a thermal chamber. Force was recorded while the thermal chamber was heated from 25°C to 80°C (to trigger activation according to Table I). Seven tests were performed using two actuators to assess the repeatability of the blocking force response within and between actuators. One actuator was tested 5 times between 25-80°C, and the second actuator was tested twice, including once up to 160°C, to determine the magnitude of stress-induced martensitic transformation that occurs beyond the temperature bounds determined in calorimetry testing. The results of these tests are shown in Fig. 7 (the data is presented as averages with 95% confidence bounds).

As can be seen in Fig. 7, the coil actuators demonstrate repeatable force generation as a function of temperature, both within and between specimens. Note that forces are generated as low as 30°C, and that force generation slope increases once

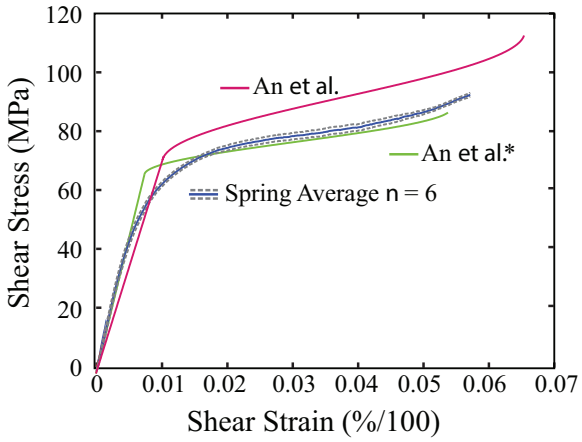

Fig. 6. De-twinning shear stress vs. shear strain. The two state model from An *et al.* is overlaid twice on the data, once using their reported parameters (referred to as An *et al.*) and once with parameters calculated from our experimental data (referred to as An *et al.**). Note that An *et al.* tested larger spring index specimens than those tested for this study, which explains the deviations in model parameters.

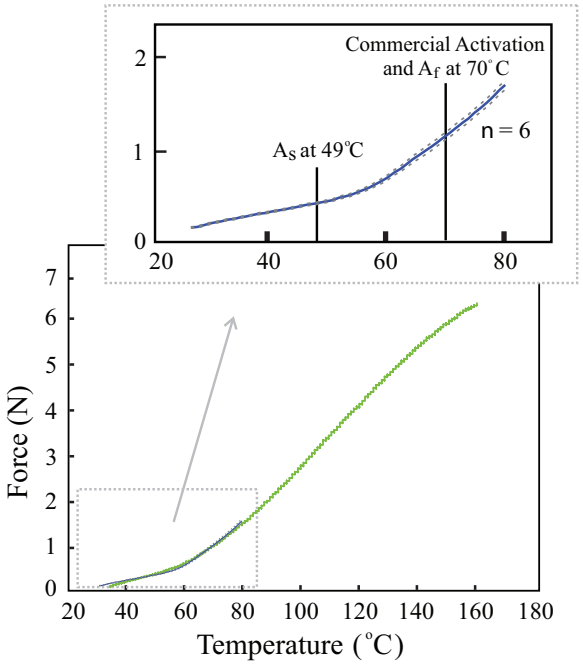

Fig. 7. Force vs. temperature for blocking force tests. Actuators were initially held at 100% their initial length, and were repeatedly heated from 25°C to 80°C (magnified above). The listed activation temperature for the Flexinol wire provided by the manufacturer (70°C), and the austenite start temperature as determined by calorimetry testing, (49°C), are included for reference. A second actuator was heated from 25°C to 160°C and is overlaid on the original data for comparison.

the actuators reach approximately 60°C (which is close, but not equal, to the reported off-the-shelf activation temperature of 70°C). Of particular interest is actuator behavior as temperature increases beyond 60°C: force continues to increase with temperature to the limit of the test window (160°C), producing maximum forces of 6.24 N. This is different than what was measured in Table I, and is indicative of stress-induced martensitic transformation (i.e., in a blocking-force configuration, the stress generated as the coil actuates induces a reverse austenite-martensite phase change, effectively increasing the critical temperature required for full austenite activation) [20], [26], [45]–[48]. This is a well-documented effect, and is well described by the Clausius-Clapeyron relation [20], [26].

This finding has several implications: when used in a real-life setting, where external stresses are present, coil force generation is a continuous response over a wide range of input temperatures that is affected by the presence and magnitude of said stress; SMA coils, when used in a blocking-force configuration, provide opportunities for precision force control through applied voltage, as the force response of the coil can be tuned continuously as a result of the extended temperature range over which the coil activates (i.e., a narrow activation temperature range results in actuators that are more difficult to control precisely); and finally, force generation models that predict maximum force generated based on the assumption of 100% austenite transformation (and therefore use pure austenite shear modulus values to calculate force) are limited in their practical predictive power if used in this regime where the transformation window is extended beyond the expected or published bounds (i.e., such models will over-predict the generated force in these cases).

D. Actuator Response and Path Dependence

For the coil actuator design discussed in this paper, the shape memory effect is utilized by first de-twinning the actuators to a given extensional strain at room temperature, and then applying a voltage to trigger resistive heating to produce a blocking force. If the steps are reversed (i.e., if the actuator is heated to trigger complete austenite activation at zero extensional strain, then stretched) the force profile and maximum force generated will differ.

This is shown in Fig. 8. De-twinning followed by blocking force resistive heating results in a maximum shear stress that is significantly lower than that measured when the same actuator is strain-cycled entirely at high temperature (235 MPa vs. 333 MPa, a decrease of 29.4%). This demonstrates that actuator performance is highly path dependent, which is important for both modeling actuator performance and for system design: compression garments require both high forces (which are most effectively achieved if the actuators are heated first then strained) and easy donning/doffing (which is most effectively achieved if the actuators are de-twinned at low temperature, then heated to constrict).

This effect is not yet fully understood, and additional study is required. It is possible that this is not actually a hysteresis effect, but is instead an example of incomplete phase transformation due to stress-induced reverse martensitic transformation unique to blocking-force activation (i.e., extending the orange path to a greater temperature level may result in active shear stress values that converge to the load-cycling value). Additional study is necessary to test this hypothesis. In the absence of a full understanding of this effect, it is prudent for system designers who intend to use the stretch-then-heat (instead of the heat-then-stretch) architecture to anticipate a potential loss in actuator performance and to upscale system

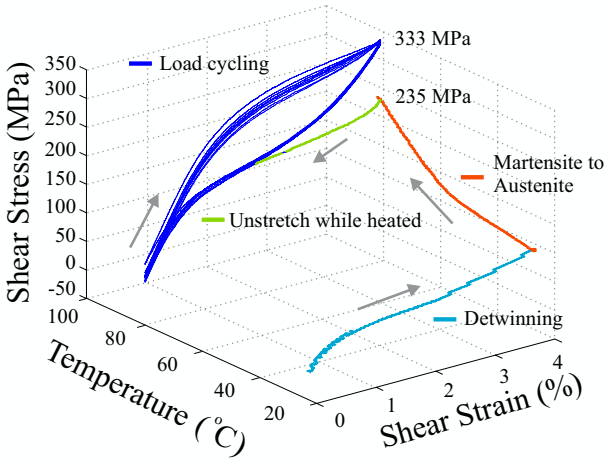

Fig. 8. Actuators de-twinned at room temperature then heated at a fixed extensional strain generate a specific shear stress value (235 MPa in this case). If the same actuators are instead displacement-cycled entirely at high temperature, a greater shear stress value (333 MPa) is measured at the same temperature-strain combination.

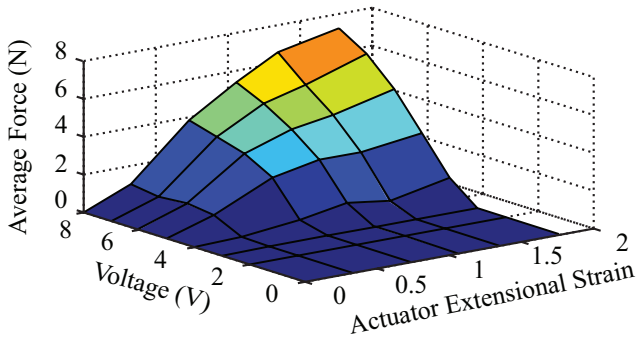

Fig. 9. Average blocking force generated by four coil actuators when exposed to a 60s applied voltage at a fixed extensional strain ϵ. Force increases as voltage increases (for a fixed ϵ) and force linearly increases (R^2 = 0.82) as ϵ increases (for a fixed voltage), which validates the force-extensional strain model for $\epsilon \leq 1.77$.

requirements accordingly.

E. Active Blocking Force-Voltage-Extensional Strain Testing

A final set of tests was completed to characterize the joint effect of extensional strain and applied voltage (and therefore applied power) on average blocking force, and to compare these results to the previously described voltage-thermal and extensional strain-force models. Four coil actuators of equal length (L_0 = 8.255 cm, n = 245 $\pm$ 3, packing density η = 0.9 $\pm$ 0.015) were each exposed to an applied voltage for 60s at a fixed extensional strain, and average steady-state blocking forces were measured. After 60s, the voltage was increased, and the test was repeated (6 applied voltages were tested, from 3-8 V). Upon completion of a full voltage sweep, each actuator was removed from the test stand and the fixed extensional strain was varied (5 total strains were tested), and the voltage sweep was repeated. Average steady state blocking force was thus measured at 30 voltage-extensional strain combinations for each actuator. Data was collected using a tabletop variable height test stand, a tunable DC voltage power supply, and a Futek LTH350 donut load cell [Futek Inc.].

Fig. 9 presents the data collected from these tests, averaged across all four actuators. We see that for a fixed extensional strain, force increases with increasing voltage up to a maximum recorded force of 7.24 N, which is consistent with the relationship from Fig. 7: voltage drives an increase in temperature, which in turn causes an increase in blocking force, and this is an extended and continuous response due to stress-induced martensite transformation. We see that for voltages $\leq$ 3 V, the heat generated is largely insufficient to trigger austenite activation (and nearly zero force is recorded). Similarly, for a fixed voltage (and therefore fixed temperature), force increases with increasing extensional strain, which is consistent with (1) and all subsequently derived force equations. Combining the findings from these results, force is maximized for a given actuator by maximizing both extensional strain (up to the point of mechanical failure) and applied voltage (up to the point that full austenite activation occurs, or the temperature exceeds the memory-resetting temperature).

F. Assessing Actuator Linearity and Thermal Model Efficacy

The prevailing SMA coil actuator force-displacement model developed by An *et al.*, which serves as the basis for many of the equations in this paper, bases its activation force predictions on the assumption that the actuator is operating within the linear region of the shear stress-shear strain curve [31]. The tests conducted in Fig. 7-9 operate at large extensional strains that may extend beyond the intended limits of such models (and many envisioned uses of SMA coils in future compression garments would require similarly large extensional strains). To assess the linearity of the coil actuators in the tests represented in Fig. 9, linear fits were matched to the extensional strain-force data (controlling for voltage), resulting in an average R^2 = 0.82 for extensional strains $\epsilon \leq 1.77$. This suggests that linear force-displacement models that are used to predict forces at large extensional strains (at least up to ϵ = 1.77) can predict actuator behavior.

To assess the efficacy of the thermal model presented in this paper, steady state temperatures were predicted using (12) and (13) for the actuators used in the voltage-blocking force tests (see Fig. 9). Force-temperature data from the thermal chamber blocking force tests (see Fig. 7) were treated as truth reference values (for ϵ = 1), and temperature values were estimated for each measurement by normalizing the measured force to a reference ϵ = 1 extensional strain, then cross-referencing this force value against the truth force-temperature table. This method is based on the assumption of force-extensional strain linearity through the extensional strain envelope of interest.

The results of this assessment are included in Fig. 10, assuming coil packing density η = 0.9, a convective heat transfer coefficient h = 90 W/(m^2°C), a specific heat C = 837.36 J/(kg°C), and a static wire austenite resistivity = 100 $\mu\Omega$-cm [49]. Fig. 10 presents the average temperature error between the model output and predicted values using the force-temperature reference method for all extensional strains as a function of voltage. The general under-prediction of the model

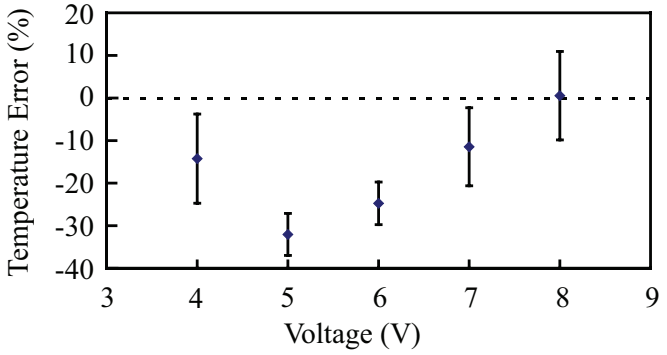

Fig. 10. Average temperature error vs. voltage, as predicted by the voltage-temperature model, compared against estimated temperatures achieved in voltage-force tests (linearly corrected for ϵ between 0.33-1.77.

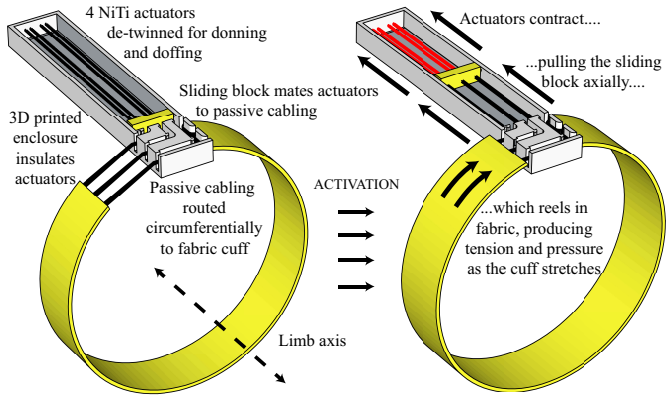

Fig. 11. Schematic of compression tourniquet using integrated NiTi coil actuators, 3D printed housing and slider block, and passive fabric.

(and the associated upward trend with increasing voltage) likely stems from limitations in the assumption that SMA resistance can be treated as simply the resistance of austenite phase NiTi: as temperature increases and a greater percentage of the material exists in the austenite phase, the wire resistance approaches the resistance of pure NiTi austenite; at lower temperatures, where this is not the case, the model will under-predict wire temperature (martensite resistivity is lower than that of austenite, so a pure martensite wire will reach higher temperatures than a pure austenite wire for a fixed voltage). This manifests as large errors in predicted blocking force at low temperatures. The small average error recorded at the lowest voltage setting, which is inconsistent with this theory, is likely a unique result of a superposition of both the resistivity error (which causes the model to under-predict temperature) and errors stemming from a non-uniform heating effect that was observed only at low voltages (leading to lower than anticipated measured actuation forces, and therefore under-estimations of temperature using the ground truth table, which artificially brings the model into closer alignment).

V. Compression Tourniquet Using Integrated NiTi Coil Actuators

A first-generation compression tourniquet was developed and tested using low spring index coil actuators that were described in the preceding sections and is depicted in Fig. 11. This prototype consisted of three subcomponents: four parallel-aligned NiTi coil actuators, to provide activation forces and displacements; a band of breathable and compliant fabric, to serve as the cuff that imparts counter-pressure on the body through tension produced by the actuators; and a 3D-printed housing structure, to isolate the actuators from the tourniquet system and to provide structure to couple the actuators to the fabric via a sliding block. This prototype is similar in concept to that depicted in Fig. 4, with the actuators aligned axially rather than circumferentially.

A. Tourniquet Design and Manufacturing

The prototype tourniquet system features several strategic design decisions. First, the NiTi coil actuators are housed in an axially-aligned 3D printed plastic compartment that physically separates the actuators from the circumferential fabric cuff that directly interacts with the wearer. Instead of direct coupling (as is the case in Fig. 4), these subcomponents are connected through an intermediate, axially-aligned free-sliding block, which is connected on one face to the actuators and on the opposing face to passive cabling that is routed through the housing structure to the cuff. The actuators are fixed to both the sliding block and the back wall of the housing using 3D printed press-fit components that are epoxied together for added grip strength. As the actuators contract, the sliding block is pulled axially up the length of the housing, which reels in and stretches the cuff around an object, creating tension and counter-pressure. Equilibrium is reached when the force generated by the actuator system is balanced by the tension from the stretched cuff as it wraps around the underlying limb.

This architecture was chosen for several reasons: to provide thermal and electrical insulation between the wearer and the actuators; to provide a compact and stable electrical path for voltage-based actuation; and also to maximize the circumferential coverage of the fabric cuff on the wearer. The sliding block contains embedded copper tape, which closes the circuit by separating the actuators into two parallel bundles, and bridging the bundles in series. The geometries of the system (i.e., the number of actuators, the extensional strain stroke length, the passive cabling length, and the desired fabric cuff stretch ratio) can be tuned for specific counter-pressure requirements, donning/doffing requirements, and/or power consumption requirements.

This system was manufactured and assembled using the following components: 4 Flexinol NiTi coil actuators (C = 3.08, d = 305 μm, average L_0 = 5.00 cm, average n = 139, average η = 0.85) produced using the method described in Fig. 5; a 3D printed housing and slider block made from acrylonitrile butadiene styrene (ABS) thermoplastic, produced using a Stratasys Fortus 250mc printer [Stratasys, Ltd.]; 200 μm diameter stainless steel passive cabling; and a 2.54 cm wide band of breathable compression fabric [BioSkin, inc.].

B. Force and Pressure Testing

Force and pressure tests were conducted using the tourniquet prototype system to determine its effectiveness at pro-

ducing counter-pressure against a rigid object (simulating a limb). Blocking force tests using the four-actuator system were shown to produce forces up to 24.75 N at 5 V (4.55 W) at an extensional strain ϵ = 1.36 (an average force per actuator of 6.19 N). The system performs as expected: previous testing of actuators at $\epsilon \approx 1.35$ at the same activation temperature (see Fig. 9) produced forces of 6.57 N, a difference of only 5.7%.

Pressure production testing was completed by wrapping the tourniquet cuff around a rigid PVC pipe (outer diameter = 11.43 cm), then applying an increasing step voltage to stretch the cuff around the pipe. This setup is represented in Fig. 12. Voltage was applied at 60s intervals, from 0-10 V, and counter-pressure between the cuff and the pipe was recorded using a Novel S2075 Pliance pressure sensor (a 15.24 cm x 15.24 cm sensor with 256 sensing pixels, range of 2-200 kPa and accuracy >95% of the measured value) [Novel Electronics, Inc.]. Two different cuff bands were tested: one measuring 20.6 cm when completely unstretched (and stretched 34% to 27.6 cm when wrapped around the pipe), and another measuring 24.1 cm (and stretched 16% to 27.9 cm when wrapped). The remaining pipe circumference was occupied by the tourniquet casing and the connective steel thread.

The results of the pressure production tests are shown in Fig. 13, and represent the average pressure produced (with 95% confidence) as a function of voltage (with curvature effects removed). The pressure production profile is significantly affected by the initial cuff parameters: the longer cuff, which required less initial stretching to be donned on the pipe (16% vs. 34% for the shorter cuff), produced less pressure at all conditions (including the 0 V condition, representing the passive pressure applied by the cuff before activation). This is consistent with expectations, as the actuator system will reach equilibrium at a smaller extensional strain when paired with a longer, less-stretched cuff, resulting in a lower circumferential tension. Conversely, the shorter cuff, which had to be stretched a greater percentage when donned (and thus produced a larger passive pressure and provided a larger resistance to the actuator system), produced greater pressure at all voltages because the final strain of the actuator system was greater (ϵ = 0.37 vs. 0.17, respectively).

In each case, the system reaches steady state as voltage is increased: for both cuffs, pressure values stabilize for voltages $\geq$ 6 V (to within $\pm$ 5.6% for the tight cuff, and $\pm$ 10.0% for the loose cuff). The steady state pressure produced is consistent with the values predicted by (10) using an estimated shear modulus G = 7.5 GPa when corrected for cycling-induced creep in L_0 (and thus changes in η and ϵ). This modulus term is lower than average [31], which is likely attributable to both fatigue effects and path dependency losses (see Fig. 8). Additionally, because each cuff is initially stretched (producing a baseline counter-pressure that does not rely on actuation), it is important to assess the magnitude of additional pressure that is produced as a result of the NiTi actuators: with the short cuff, steady state activation equilibrium produces 6.05 kPa (compared to 3.45 kPa when deactivated), an increase of 75%; with the long cuff, activation produces 1.85 kPa (compared to 0.49 kPa when deactivated), an increase of 277%.

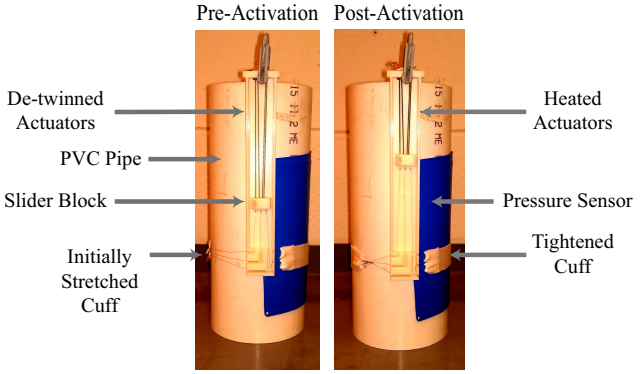

Fig. 12. Initial pressure testing setup. The prototype tourniquet cuff is stretched circumferentially around a PVC pipe, with the actuators and housing held orthogonally along its length. The pressure sensor mat is placed underneath the cuff on the surface of the pipe. Note that the position of the pressure sensor in this figure is for illustrative purposes: the sensor was placed exactly opposite the actuator housing during testing.

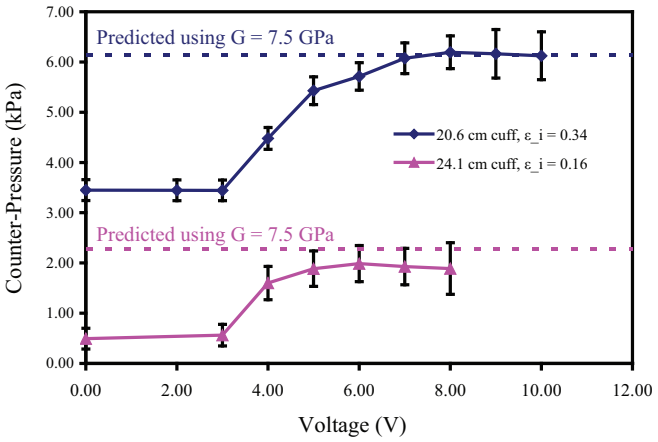

Fig. 13. Prototype active tourniquet pressure production as a function of voltage, for two different initial cuff sizes, with predicted values.

VI. Discussion

The performance of the prototype tourniquet system provides several insights into future system design. First, the system clearly augments the performance of a typical passive cuff, as we measured significant increases in counter-pressure over baseline as a result of activation. It is also clear that the amount of initial tension in the cuff affects the magnitude of additional counter-pressure that can be produced by the actuator system. To produce maximum forces (and pressures), the effective spring index and/or initial tension of the passive cuff should be sufficiently large to block the actuators during activation. However, this comes at the cost of easy donning/doffing.

Based on these findings, the prototype tourniquet system can be significantly improved with minor modifications. Reducing the packing density of the coil actuators, increasing the number of parallel actuators, and further shortening the initial length of the passive cuff (or choosing a material with higher stiffness) would all lead to higher counter-pressure levels than those measured in this study. Each of these changes would push the system performance higher, as predicted by (10). The housing used to isolate the actuators could also be considerably reduced

in size with improved manufacturing and assembly methods, and a passive locking mechanism could be implemented to catch the slider block after actuation to maintain the applied pressure without the need of continuous power. Finally, smart sensors (e.g., a piezoelectric film) could be applied to the inner cuff layer to act as in-situ pressure monitors, providing feedback to the voltage control system to precisely control applied pressure.

Finally, it is important to note that the novel prototype system presented in this study is only one of several viable architectures for compression garment design using low spring index NiTi coil actuators. The tourniquet approach falls under a category we call hybrid garments – passive textile structures that are manipulated at the seams by actuators and lightweight support structures to produce a meta-garment with shape changing and compression properties – of which several other designs are possible. An alternative approach, and one that is of particular interest going forward, is the production of textile structures that actually make use of these actuators as integrated textile elements (where instead of using the actuators as manipulators of traditional passive textiles, they themselves form the textile structure). Low spring index NiTi coil actuators are well suited for this type of design, as they can produce large displacements and large forces in a form factor that closely resembles a typical textile fiber (with low mass and bulk penalties). This type of development opens up possibilities of specialized woven, knit, braided, and other textiles with unique and interesting shape change properties. Such garments could prove useful for a multitude of applications beyond compression garments, including things like streamlined assistive or restrictive exoskeleton systems [50]–[53]. Research on these designs is ongoing.

While much effort was dedicated to fundamentally characterize the performance of the low spring index actuators, additional aspects of actuator behavior require further study. Cycling and fatigue effects are a known limitation of shape memory alloys [20], and the susceptibility of these actuators to cycle-based performance degradation is important to quantify. Performance sensitivities to manufacturing (e.g., Flexinol vs. as-drawn Nitinol), annealing temperature, and alloy content also warrant further study. Finally, textiling and manufacturing challenges remain (as many textile machines are not designed to process coiled metal alloys). A viable manufacturing approach that warrants additional study is to combine low spring index coil actuators with 3D printed structures (as was the case in the tourniquet prototype system) to produce either traditional (e.g., weave, knit, or braid) or hybrid (e.g., tourniquet-style) meta-structures. Customized systems using this approach could incorporate multiple materials, stiffnesses, and complexities, opening up design possibilities that may not be achievable with typical industrial textiling equipment.

Ultimately, this study demonstrates that compression garments need not be limited to passive, difficult to don garments or bulky pneumatic solutions: low spring index NiTi coil actuators offer a low mass, low bulk, large displacement, and large force solution to improve compression garment performance, both in terms of maximum pressure production and ease of donning/doffing. This approach to design can be utilized in a wide variety of applications, from healthcare stockings to cosmetic shapewear to advanced MCP space suits.

ACKNOWLEDGMENT

The authors would like to thank Lindsay Aitchison, Prof. Chris Schuh, Dr. Tricia Wilson, Dr. Leah Buechley, Sunny Wicks, and Nora Newie for their contributions to this study.

REFERENCES

[1] C. Diehm, H. Trampisch, S. Lange, and C. Schmidt, "Comparison of leg compression stocking and oral horse-chestnut seed extract therapy in patients with chronic venous insufficiency," *The Lancet*, vol. 347 (8997), pp. 292–294, 1996.

[2] M. J. Brennan and L. T. Miller, "Overview of treatment options and review of the current role and use of compression garments, intermittent pumps, and exercise in the management of lymphedema," *Cancer*, vol. 83, no. S12B, pp. 2821–2827, 1998.

[3] B. Doan, Y.-H. Kwon, R. Newton, J. Shim, E. Popper, R. Rogers, L. Bolt, M. Robertson, and W. Kraemer, "Evaluation of a lower-body compression garment," *J. Sports Sci.*, vol. 21, pp. 601–610, 2003.

[4] T.-L. Teng and K.-T. Chou, "The measurement and analysis of the pressure generated by burn garments," *J. Med. and Biological Eng.*, vol. 26 (4), pp. 155–159, 2006.

[5] J. Kragh Jr., M. Littrel, J. Jones, T. Walters, D. Baer, C. Wade, and J. Holcomb, "Battle casualty survival with emergency tourniquet use to stop limb bleeding," *J. Emergency Med.*, vol. 41 (6), pp. 590–597, 2011.

[6] S. Platts, J. Tuxhorn, L. C. Ribeiro, M. Stenger, S. Lee, and J. Meck, "Compression garments as countermeasures to orthostatic intolerance," *Aviation, Space, Environ. Med.*, vol. 80, no. 5, pp. 437–442, 2009.

[7] P. Webb and J. Annis, "The principle of the space activity suit," *NASA CR-973*, 1967.

[8] J. Waldie, K. Tanaka, D. Tourbier, P. Webb, C. Jarvis, and A. Hargens, "Compression under a mechanical counter pressure space suit glove," *J. Grav. Physiol.*, vol. 9 (2), pp. 93–98, 2002.

[9] D. Newman, J. Hoffman, K. Bethke, C. Carr, N. Jordan, L. Sim, N. Campos, C. Conlee, B. Smith, J. Wilcox, G. Trotti, and Mide-Technologies, "Astronaut bio-suit system for exploration class missions," *NIAC Phase II Final Rep.*, 2005.

[10] D. Judnick, D. Newman, and J. Hoffman, "Modeling and testing of a mechanical counterpressure bio-suit system," in *Int. Conf. Environmental Syst.*, 2007, pp. 2007–01–3172.

[11] K. Tanaka, P. Danaher, P. Webb, and A. Hargens, "Mobility of the elastic counterpressure space suit glove," *Aviation, Space, Environ. Med.*, vol. 80 (10), pp. 890–893, 2009.

[12] J. Madden, N. Vandesteeg, P. Anquetil, P. Madden, A. Takshi, R. Pytel, S. Lafontaine, P. Wieringa, and I. Hunter, "Artificial muscle technology: physical principles and naval prospects," *IEEE J. Ocean. Eng.*, vol. 29 (3), pp. 706–728, 2004.

[13] S.-K. Lee, S.-J. Lee, H.-J. An, S.-E. Cha, J. K. Chang, B. K. Kim, and J. J. Pak, "Biomedical applications of electroactive polymers and shape memory alloys," in *Proc. SPIE*, vol. 4695, 2002, pp. 17–31.

[14] C. Haines, M. Lima, N. Li, G. Spinks, J. Foroughi, J. Madden, S. H. Kim, S. Fang, M. J. de Andrade, F. Goktepe, O. Goktepe, S. Mirvakili, S. Naficy, X. Lepro, J. Oh, M. Kozlov, S. J. Kim, X. Xu, B. Swedlove, G. Wallace, and R. Baughman, "Artificial muscles from fishing line and sewing thread," *Science*, vol. 343, pp. 868–872, 2014.

[15] B. Holschuh, E. Obropta, L. Buechley, and D. Newman, "Materials and textile architecture analyses for mechanical counter-pressure space suits using active materials," in *AIAA Space 2012 Conf. Expo.*, 2012.

[16] S. Ahmadi, A. C. Mattos, A. Barbazza, M. Soleimani, P. Boscariol, and C. Menon, "Fabrication and performance analysis of a dea cuff designed for dry-suit applications," *Smart Materials and Structures*, vol. 22, no. 3, p. 035002, 2013.

[17] J.-S. Plante and S. Dubowsky, "On the nature of dielectric elastomer actuators and its implications for their design," in *Smart Structures and Materials 2006: Electroactive Polymer Actuators and Devices (EAPAD)*, vol. 6168. SPIE, 2006, pp. 61 681J–1 – 61 681J–11.

[18] N. Newie, "Investigation of active materials for use in mechanical counter-pressure space suits," Master's thesis, Technical University of Munich, 2013.

[19] B. Wee, "Assessment and preliminary model development of shape memory polymer mechanical counter pressure space suits," Undergraduate Thesis, Massachusetts Institute of Technology, 2013.

[20] D. C. Lagoudas, *Shape memory alloys: modeling and engineering applications*. Springer, 2008.
[21] F. El Feninat, G. Laroche, M. Fiset, and D. Mantovani, "Shape memory materials for biomedical applications," *Adv. Eng. Mater.*, vol. 4 (3), pp. 91–104, 2002.
[22] Y. Haga, Y. Tanahashi, and M. Esashi, "Small diameter active catheter using shape memory alloy," *Proc., 11th Annu. Int. Workshop Microelectromech. Syst.*, pp. 419–424, 1998.
[23] B. Kim, M. G. Lee, Y. P. Lee, Y. Kim, and G. Lee, "An earthworm-like micro robot using shape memory alloy actuator," *Sens. Actuators A*, vol. 125, no. 2, pp. 429–437, 2006.
[24] C. Pfeiffer, K. De Laurentis, and C. Mavroidis, "Shape memory alloy actuated robot prostheses: initial experiments," in *1999 IEEE Int. Conf. Robot. Autom.*, 1999, pp. 2385–2391.
[25] S. Seok, C. Onal, K.-J. Cho, R. Wood, D. Rus, and S. Kim, "Meshworm: A peristaltic soft robot with antagonistic nickel titanium coil actuators," *IEEE/ASME Trans. Mechatron.*, vol. 18 (5), pp. 1485–1497, 2012.
[26] L. Stirling, C.-H. Yu, J. Miller, E. Hawkes, R. Wood, E. Goldfield, and R. Nagpal, "Applicability of shape memory alloy wire for an active, soft orthotic," *J. Mater. Eng. Performance*, vol. 20 (4-5), pp. 658–662, 2011.
[27] K. Yang and C. Gu, "A novel robot hand with embedded shape memory alloy actuators," *J. Mech. Eng. Sci.*, vol. 216, pp. 737–745, 2002.
[28] R. Johnson, J. Padgett, M. E. Maragakis, R. DesRoches, and M. S. Saiidi, "Large scale testing of nitinol shape memory alloy devices for retrofitting of bridges," *Smart Mater. Struct.*, vol. 17, no. 3, 2008.
[29] M. D. Pierce and S. A. Mascaro, "A biologically inspired wet shape memory alloy actuated robotic pump," *IEEE/ASME Trans. Mechatron.*, vol. 18 (2), pp. 536–546, 2012.
[30] J. Berzowska and M. Coelho, "Kukkia and vilkas: Kinetic electronic garments," *9th IEEE Int. Symp. Wearable Comput.*, 2005.
[31] S. M. An, J. Ryu, M. Cho, and K. J. Cho, "Engineering design framework for a shape memory alloy coil spring actuator using a static two-state model," *Smart Mater. Struct.*, vol. 21 (5), 2012.
[32] S. Kim, E. Hawkes, K. Cho, M. Jolda, J. Foley, and R. Wood, "Micro artificial muscle fiber using niti spring for soft robotics," in *2009 IEEE/RSJ Int. Conf. Intell. Robots Syst.*, 2009, pp. 2228–2234.
[33] H. Lee and J. Lee, "Evaluation of the characteristics of a shape memory alloy spring actuator," *Smart Mater. Struct.*, vol. 9, no. 6, p. 817, 2000.
[34] Z. Wang, X. Zu, X. Feng, S. Zhu, J. Bao, and L. Wang, "Characteristics of two-way shape memory tini springs driven by electrical current," *Mater. and Des.*, vol. 25 (8), pp. 699–703, 2004.
[35] C. D. Onal, R. J. Wood, and D. Rus, "An origami-inspired approach to worm robots," *IEEE/ASME Trans. Mechatron.*, vol. 18 (2), pp. 430–438, 2012.
[36] J.-S. Koh and K.-J. Cho, "Omega-shaped inchworm-inspired crawling robot with large-index-and-pitch (lip) sma spring actuators," *IEEE/ASME Trans. Mechatron.*, vol. 18 (2), pp. 419–429, 2012.
[37] M. Paredes, M. Sartor, and C. Masclet, "An optimization process for extension spring design," *Comput. Methods Appl. Mechanics and Eng.*, vol. 191, no. 8, pp. 783–797, 2001.
[38] J. A. Collins, H. R. Busby, and G. H. Staab, *Mechanical design of machine elements and machines*. John Wiley and Sons, 2009.
[39] R. G. Budynas and J. K. Nisbett, *Shigley's mechanical engineering design*. McGraw-Hill New York, 2008.
[40] NASA, "Human integration design handbook (hidh)," NASA/SP-2010-3407, Tech. Rep., 2010.
[41] D. R. Madill and D. Wang, "Modeling and l2-stability of a shape memory alloy position control system," *IEEE Trans. Control Syst. Technol.*, vol. 6, no. 4, pp. 473–481, 1998.
[42] Y. H. Teh, *Fast, Accurate Force and Position Control of Shape Memory Alloy Actuators*. Australian National University, 2008.
[43] Y. Tadesse, N. Thayer, and S. Priya, "Tailoring the response time of shape memory alloy wires through active cooling and pre-stress," *J. Intell. Mater. Syst. Struct.*, vol. 21, pp. 19–40, 2010.
[44] K. Ikuta, M. Tsukamoto, and S. Hirose, "Mathematical model and experimental verification of shape memory alloy for designing micro actuator," in *IEEE Proc. Microelectromech. Syst.*, 1991, pp. 103–108.
[45] A. McKelvey and R. Ritchie, "On the temperature dependence of the superelastic strength and the prediction of the theoretical uniaxial transformation strain in nitinol," *Philosoph. Mag. A*, vol. 80, no. 8, pp. 1759–1768, 2000.
[46] K. Ng and Q. Sun, "Stress-induced phase transformation and detwinning in niti polycrystalline shape memory alloy tubes," *Mechanics of Mater.*, vol. 38 (1), pp. 41–56, 2006.
[47] Y. Liu, "Detwinning process and its anisotropy in shape memory alloys," *Smart Mater. MEMS*, vol. 4234, pp. 82–93, 2001.
[48] Y. Chen and C. Schuh, "Size effects in shape memory alloy microwires," *Acta Materialia*, vol. 59, pp. 537–553, 2011.
[49] H. Song, E. Kubica, and R. Gorbet, "Resistance modelling of sma wire actuators," in *Smart Mater. Struct. and NDT in Aerosp.*, 2011.
[50] P. K. Jamwal, S. Q. Xie, S. Hussain, and J. G. Parsons, "An adaptive wearable parallel robot for the treatment of ankle injuries," *IEEE/ASME Trans. Mechatron.*, vol. 19 (1), pp. 64–75, 2012.
[51] C. Jones, F. Wang, R. Morrison, N. Sarkar, and D. Kamper, "Design and development of the cable actuated finger exoskeleton for hand rehabilitation following stroke," *IEEE/ASME Trans. Mechatron.*, vol. 19 (1), pp. 131–140, 2012.
[52] K. Kong and D. Jeon, "Design and control of an exoskeleton for the elderly and patients," *IEEE/ASME Trans. Mechatron.*, vol. 11, no. 4, pp. 428–432, 2006.
[53] J. C. Perry, J. Rosen, and S. Burns, "Upper-limb powered exoskeleton design," *IEEE/ASME Trans. Mechatron.*, vol. 12, no. 4, pp. 408–417, 2007.

Bradley Holschuh received the Bachelor of Science degree in aerospace engineering in 2007, the Masters of Science degree in aeronautics and astronautics in 2010, the Masters of Science degree in technology and policy in 2010, and the Doctor of Philosophy degree in aerospace biomedical engineering in 2014, all from the Massachusetts Institute of Technology (MIT).

He is currently a Post-doctoral Associate in the Man-Vehicle Laboratory in the Department of Aeronautics and Astronautics at MIT. He was part of the 2011 class of NASA Space Technology Research Fellows (NSTRF), and is a student member of the American Institute of Aeronautics and Astronautics (AIAA). His research interests include bioastronautics, extravehicular activity (EVA), and active materials and textiles.

Edward Obropta received the Bachelor of Science degree in aerospace engineering in 2013, and is currently pursuing a Masters of Science degree in aeronautics and astronautics, from the Massachusetts Institute of Technology (MIT).

He is a student member of the American Institute of Aeronautics and Astronautics (AIAA). His research interests include bioastronautics, space suit design, structural mechanics, active materials, electronic textiles, and sports technology.

Dava Newman received the Bachelor of Science degree in aerospace engineering from the University of Notre Dame in 1986, the Masters of Science degree in aeronautics and astronautics in 1989, and the Masters of Science degree in technology and policy in 1989, and the Ph.D. degree from the Massachusetts Institute of Technology (MIT) in aerospace biomedical engineering in 1992.

She is currently a Professor in the Department of Aeronautics and Astronautics and Engineering Systems at MIT and affiliate faculty in the Harvard-MIT Health Sciences and Technology Program. She leads research efforts in extravehicular activity (EVA) including advanced space suit design, musculoskeletal modeling, biomechanics and energetics, human-robotic cooperation, and biomedical devices. Her exoskeleton innovations are now being applied to "soft suits" to study and enhance locomotion on Earth for children with Cerebral Palsy in addition to astronauts.